

Error Performance Characterization of LoRa-Based Direct-to-Satellite IoT

Quantao Yu, Deepak Mishra, *Senior Member, IEEE*, Hua Wang, *Member, IEEE*,
Dongxuan He, *Member, IEEE*, Jinhong Yuan, *Fellow, IEEE*, and Michail Matthaiou, *Fellow, IEEE*

Abstract—Recently, Long-Range (LoRa) based direct-to-satellite Internet-of-Things (DtS-IoT) has garnered widespread attention from both academia and industry due to its capability to provide pervasive connectivity in an energy-efficient and cost-effective manner. A rigorous error performance analysis of such a new paradigm is quite essential for future green IoT communications. In this paper, we provide a novel analytical framework to characterize the error performance of LoRa-based DtS-IoT systems by leveraging an empirically-verified satellite-to-ground channel model. To enable a realistic performance analysis, non-coherent detection is considered in the presence of interference along with the relative time and frequency offsets, where the corresponding decision metrics are theoretically derived. Based on this, closed-form symbol and bit error rate expressions are obtained by approximating the impact of the overall interference distributed within the decision metrics by that of the peak interference. Moreover, the impact of some key system parameters, such as the spreading factor (SF), bandwidth, and the end-device's (ED's) location, on the error performance is thoroughly investigated. The validity of our theoretical analysis is substantiated by extensive numerical simulations, where further insights are obtained into the error performance improvements of LoRa-based DtS-IoT.

Index Terms—Direct-to-satellite IoT (DtS-IoT), error performance, green IoT, LoRa.

I. INTRODUCTION

WITH the rapid growth of Internet-of-Things (IoT) services, pervasive connectivity and green communications are becoming more and more important towards the realization of fully intelligent societies [2]. In this context, Long-Range (LoRa) based direct-to-satellite IoT (DtS-IoT) has been regarded as a promising approach to provide ubiquitous coverage in an energy-efficient and cost-effective manner, which has attracted a lot of research interest as well as commercial traction [3], [4]. For example, the authors in [5], [6] verified the feasibility of LoRa-based radio links in low Earth orbit (LEO) satellite communications under the impact of Doppler effect through both laboratory testings and outdoor experiments. The authors in [7] assessed LoRa for satellite-to-Earth communications considering the impact of ionospheric

Q. Yu, H. Wang, and D. He are with Beijing Institute of Technology, Beijing 100081, China, (e-mails: 3120215432@bit.edu.cn; wanghua@bit.edu.cn; dongxuan_he@bit.edu.cn).

D. Mishra and J. Yuan are with the School of Electrical Engineering and Telecommunications, University of New South Wales Sydney, NSW 2052, Australia, (e-mails: d.mishra@unsw.edu.au; j.yuan@unsw.edu.au).

M. Matthaiou is with the Centre for Wireless Innovation (CWI), Queen's University Belfast, BT3 9DT Belfast, U.K., (e-mail: m.matthaiou@qub.ac.uk).

A preliminary six-page conference version of this work has been submitted to the IEEE GLOBECOM 2025 for presentation [1].

scintillation. Moreover, some international organizations and satellite companies have participated in LoRa-based DtS-IoT industrial initiatives over the past few years, like Inmarsat and Lacuna Space [2], [8]. In addition, various methods have been proposed to improve the link-level and/or system-level performance of LoRa-based DtS-IoT systems, either from the physical (PHY) layer perspective like chirp spread spectrum (CSS) based waveform design [9]–[12] and signal detection [13]–[16], or from the medium access control (MAC) layer perspective like random access (RA) based protocol design [17]–[19]. Although LoRa-based DtS-IoT systems have been widely investigated, there are few studies focusing on a rigorous error performance analysis of such a new paradigm.

A. State-of-the-Art

In recent years, several studies have presented a detailed mathematical description of LoRa modulation, facilitated by reverse engineering. Specifically, Vangelista [20] first gave a digital signal processing description of LoRa modulation and provided a theoretical derivation of the optimum receiver based on discrete Fourier transform (DFT). Furthermore, the authors in [21] provided a more accurate characterization of the LoRa signal model, including its continuous and discrete analytical expressions in both time and frequency domains. Moreover, Pasolini [22] further analyzed the signal properties of LoRa modulation and their impact on transmitter and receiver architectures. To quantitatively describe the bit error rate (BER) performance of LoRa modulation under different conditions, researchers have conducted various studies considering the impact of noise, interference, channel fading, and synchronization offset. The initial study began with a curve fitting method used in [23] to estimate the BER of CSS modulation under the impact of additive white Gaussian noise (AWGN). Using a moment matching method, Elshabrawy and Robert [24] derived closed-form approximations for the BER performance of LoRa modulation considering non-coherent detection over both AWGN and Rayleigh fading channels. Then, by deriving an upper bound on the cross-correlation between two LoRa signals with the same spreading factor (co-SF), the approximate BER performance of LoRa modulation considering non-coherent detection under both AWGN and co-SF interference was derived in [25]. Furthermore, by extending the interference model in [25] to the more general case where the interfering signal is neither chip- nor phase-aligned with the desired signal, the authors in [26] derived both exact and approximate analytical expressions for the symbol error rate

TABLE I
RELATED WORKS ON ERROR PERFORMANCE ANALYSIS OF LORA-BASED SYSTEMS.

Reference	Main work	Detection
[23]	Estimated the BER of CSS modulation using a curve fitting method	—
[24]	Derived closed-form BER approximations over AWGN and Rayleigh fading channels using a moment matching method	Non-coherent
[25]	Derived approximate BER expression under AWGN and co-SF interference based on a cross-correlation upper bound	Non-coherent
[26]	Derived both exact and approximate BER expressions under AWGN and co-SF interference based on a general interference model	Non-coherent
[27]	Derived exact BER expressions over Nakagami, Rayleigh, and Rician fading channels	Non-coherent
[28]	Estimated the theoretical BER over Nakagami and Rician fading channels based on Marcum function	Non-coherent
[29]	Derived exact single integral expressions and approximate closed-form expressions for BER performance over generalized fading channels	Non-coherent
[30]	Analyzed the theoretical BER performance over two-tap and exponential decay channel models using Gauss-Hermite quadrature methods	Coherent Non-coherent
[31]	Derived approximate BER performance over heavy multi-path channels with Gaussian Q-function	Coherent Non-coherent
[32]	Analyzed the approximate BER performance under the impact of CFO with Gaussian Q-function	Coherent Non-coherent
[33]	Proposed a STBC-MIMO LoRa system and analyzed its theoretical BER performance over Rayleigh fading channels	Non-coherent
[34]	Considered a two-hop AF relaying LoRa system and analyzed its theoretical BER performance over Nakagami- m fading channels	Non-coherent
[35]	Considered a LoRa backscatter system and derived its closed-form SER expressions over AWGN and double Nakagami- m fading channels	Non-coherent
[36]	Proposed a RIS assisted LoRa system and derived its closed-form BER expressions over Rayleigh fading channels	Non-coherent
[37]	Proposed a RIS assisted LoRa system and derived its closed-form BER expressions over Nakagami- m fading channels with co-SF interference	Coherent Non-coherent
[38]	Considered a multi-RIS-aided LoRa system and derived its closed-form BER expressions with the impact of outdated and imperfect CSI	Coherent Non-coherent
[39]	Proposed a LoRa enabled AF aerial relay system and derived its exact SER expressions over SR fading channels	Non-coherent
Our work	Considered a LoRa-based DTS-IoT system and analyzed its approximate error performance in the presence of interference with synchronization offsets	Non-coherent

(SER) and BER of LoRa modulation considering non-coherent detection in the presence of AWGN and co-SF interference.

Additionally, the BER performance of LoRa modulation over typical fading channels has also been widely investigated. Exact BER expressions for non-coherent detection of LoRa modulation over Nakagami, Rayleigh, and Rician fading channels were derived in [27]. To reduce the approximation error and computational complexity, theoretical BER expressions based on Marcum function were proposed in [28] considering non-coherent detection over Nakagami and Rician fading channels. Besides, both exact single integral expressions as well as approximate closed-form expressions for the BER performance of LoRa modulation considering non-coherent detection over generalized fading channels were derived in [29]. The theoretical BER performance of LoRa modulation in multi-path frequency selective fading channels

was investigated in [30], where the error performance for both coherent and non-coherent detection was analyzed with Gauss-Hermite quadrature methods over the two-tap and the exponential decay channel models. Furthermore, the approximate BER performance of LoRa modulation over heavy multi-path channels was evaluated in [31] for both coherent and non-coherent detection with Gaussian Q-functions. By adopting a similar method as in [31], the approximate BER performance of LoRa modulation under the impact of carrier frequency offset (CFO) was analyzed in [32].

Moreover, the BER performance analysis of LoRa-based systems has been extended to more specific application scenarios [33]–[39]. In [33], a new space-time block coding multiple-input multiple-output (STBC-MIMO) LoRa system was proposed and its theoretical BER performance was analyzed over Rayleigh fading channels. In [34], the authors considered a

two-hop amplify-and-forward (AF) relaying LoRa system and derived the analytical BER expressions over Nakagami- m fading channels. Additionally, the authors in [35] derived the SER of LoRa backscatter communication systems over both AWGN and double Nakagami- m fading channels. A reconfigurable intelligent surface (RIS) assisted LoRa system was proposed in [36] and closed-form expressions for its BER and throughput were derived over Rayleigh fading channels. Furthermore, a RIS enabled anti-interference LoRa system was considered in [37], where closed-form BER expressions were derived over Nakagami- m fading channels in the presence of co-SF interference. More recently, a multi-RIS-aided LoRa system was considered in [38], where closed-form BER expressions were derived over Nakagami- m fading channels under the impact of outdated and imperfect channel state information (CSI) for both coherent and non-coherent detection. Besides, LoRa-enabled aerial communications have also come into the eyesight of researchers, where the BER performance of a LoRa enabled AF aerial relay system was investigated in [39] over shadowed Rician (SR) fading channels for non-coherent detection.

B. Motivation and Contributions

Herein, all the existing works related to the error performance analysis of LoRa-based systems are summarized in Table I for the readers' convenience. To the best of our knowledge, a rigorous error performance analysis of LoRa-based DtS-IoT systems is still lacking in the literature, which however would be quite important for the practical implementation and quantitative evaluation of such a new paradigm. Motivated by this, we provide a novel analytical framework to derive closed-form error rate expressions for LoRa-based DtS-IoT systems, which can be very helpful in facilitating system engineering design and seamless connectivity for various IoT applications especially in rural and remote areas, such as smart agriculture, environmental monitoring, asset tracking, and so on. The main contributions of this paper are summarized as follows:

- 1) A new analytical framework for characterizing the error performance (i.e., SER and BER) of LoRa-based DtS-IoT systems is developed by leveraging an empirically-verified satellite-to-ground channel model. To enable a realistic performance analysis, non-coherent detection is considered in the presence of interference along with the relative time and frequency offsets, where the corresponding decision metrics are analytically derived.
- 2) By exploiting the frequency domain peak index decision properties of non-coherent detection for LoRa modulation, the impact of the overall interference distributed within the decision metrics is approximated by that of the peak interference. Moreover, closed-form symbol and bit error rate expressions are derived using a moment matching method, where the first and second moments of the fitting random variable are theoretically derived.
- 3) The impact of some key system parameters, such as the SF, the bandwidth, and the end-device's (ED's) location, on the error performance of our considered LoRa-based

DtS-IoT system is thoroughly investigated. Extensive numerical simulations are conducted, which not only validate the accuracy our theoretical analysis but also provide further insights into the error performance improvements of such a new paradigm.

C. Paper Organization and Notations

The rest of this paper is organized as follows: The LoRa modulation is briefly introduced in Section II. Section III presents the system model and Section IV conducts the error performance analysis. Numerical results are presented in Section V, while Section VI concludes the whole paper.

Notation: Throughout this paper, we denote $F_X(x)$ and $f_X(x)$ as the cumulative distribution function (CDF) and the probability density function (PDF) of a random variable X ; $\mathbb{P}\{\cdot\}$ and $\mathbb{E}[\cdot]$ represent the probability measure and mathematical expectation, respectively; $\max\{\cdot\}$, $\exp(\cdot)$, $\ln(\cdot)$, (\cdot) , and $\Re\{\cdot\}$ are the maximum, natural exponential, natural logarithm, binomial coefficient, and real part operations; $|\cdot|$ denotes the modulus of a complex number and the cardinality of a set; $\mathcal{CN}(\cdot, \cdot)$ and $\mathcal{N}(\cdot, \cdot)$ represent the complex and real Gaussian distributions, respectively. Finally, $Q(\cdot)$ is the Gaussian Q-function.

II. PRELIMINARIES

LoRa adopts CSS modulation with the following two important parameters:

- B is the bandwidth of the LoRa modulation signal, which is typically set to be 125 kHz, 250 kHz, or 500 kHz.
- k is the SF of LoRa modulation ranging from 7 to 12, which determines the processing gain and the number of information bits within each modulation symbol (i.e., each chirp).

Under Nyquist sampling, each chirp can be defined by $M = 2^k$ samples in the complex base-band equivalent form, and the basic upchirp can be expressed as [21]

$$u[n] = \exp \left\{ j \frac{\pi n^2}{M} \right\} \exp \{-j\pi n\}, \quad (1)$$

where $n = 0, 1, \dots, M - 1$ is the sample index.

Given a SF k , LoRa is an M -ary orthogonal modulation scheme where M orthogonal upchirps are used to represent the modulation symbols. Without loss of generality, every k information bits b_0, b_1, \dots, b_{k-1} are mapped to a data symbol as $m = \sum_{i=0}^{k-1} b_i 2^i \in \mathcal{L} = \{0, 1, \dots, M - 1\}$, and thereby the modulation signal is given by [21]

$$\begin{aligned} s_m[n] &= u[n] \exp \left\{ j \frac{2\pi mn}{M} \right\} \\ &= \exp \left\{ j \frac{\pi n^2}{M} \right\} \exp \left\{ j \frac{2\pi mn}{M} \right\} \exp \{-j\pi n\}. \end{aligned} \quad (2)$$

After passing through a AWGN channel, the received signal can be expressed as

$$r_m[n] = s_m[n] + w[n], \quad (3)$$

where $w[n]$ is the complex circularly symmetric additive white Gaussian noise with zero mean and variance σ_q^2 .

Then, the signal detection for each modulation symbol can be divided into three steps, i.e., dechirp, DFT, and frequency domain (FD) peak index decision [40]. Specifically, the received signal is first multiplied by the complex conjugate of the basic upchirp, i.e., dechirp operation, and then an M -point DFT operation is performed on the dechirped signal, yielding

$$\begin{aligned} R_m[l] &= \sum_{n=0}^{M-1} r_m[n] u^*[n] \exp \left\{ -j \frac{2\pi ln}{M} \right\} \\ &= \begin{cases} M + W[m], & l = m, \\ W[l], & l \neq m, \end{cases} \quad (4) \end{aligned}$$

where $W[l] = \sum_{n=0}^{M-1} w[n] u^*[n] \exp \left\{ -j \frac{2\pi ln}{M} \right\} \sim \mathcal{CN}(0, \sigma^2)$ with $\sigma^2 = M\sigma_q^2$.

Finally, the data symbol can be estimated as [40]

$$\hat{m} = \arg \max_{l \in \mathcal{L}} \Re \{R_m[l]\}, \quad (5)$$

for coherent detection and

$$\hat{m} = \arg \max_{l \in \mathcal{L}} |R_m[l]|, \quad (6)$$

for non-coherent detection, respectively. Since coherent detection requires accurate phase synchronization, which could considerably increase the receiver's complexity and thus may not be feasible for many low-cost IoT EDs in energy-efficient communications [40]. Hence, we only consider the practical non-coherent detection in this paper, which is more attractive for green communications in our considered LoRa-based DtS-IoT systems.

III. SYSTEM MODEL

In this section, we present the system model of LoRa-based DtS-IoT, including the network model, channel model and signal model.

A. Network Model

An illustration of the network model for our considered LoRa-based DtS-IoT system is shown in Fig. 1, where an onboard gateway communicates with the desired ED on the ground directly. Without loss of generality, we denote H as the orbit altitude of the serving satellite and the satellite footprint is determined by the effective beamwidth of serving satellite, which corresponds to the maximum satellite-centric angle ψ . Moreover, there are other interfering LoRa EDs distributed within the satellite footprint, which may cause interference to the desired LoRa ED. However, it has been shown in [41] that different SFs have an average rejection signal-to-interference ratio (SIR) threshold of -16 dB. Therefore, different SFs can be considered to be quasi-orthogonal in LoRa systems and they are often used as orthogonal logical channels for different EDs [37]. Hence, we can only consider the impact of dominant co-SF interference on the system error performance. Furthermore, as stated in [37], [42], the impact of accumulative interference caused by multiple co-SF EDs can be effectively approximated by that of one dominant co-SF interfering ED in a relatively

sparse deployment scenario. Accordingly, we only consider the impact of one co-SF interfering ED in this paper¹.

Moreover, we use the contact angle φ to denote the relative location between an ED and the serving satellite, i.e., the Earth-centered zenith angle. According to the basic sine theorem, the maximum contact angle φ_m can be derived as [43]

$$\varphi_m(\psi) = \begin{cases} \sin^{-1} \left(\frac{R+H}{R} \sin \left(\frac{\psi}{2} \right) \right) - \frac{\psi}{2}, & \text{if } \psi < \psi_0, \\ \cos^{-1} \left(\frac{R}{R+H} \right), & \text{if } \psi \geq \psi_0, \end{cases} \quad (7)$$

where R is the radius of Earth and $\psi_0 = 2 \sin^{-1} \left(\frac{R}{R+H} \right)$ denotes the effective beamwidth that corresponds to just covering the horizon. Given the contact angle φ , the distance between an ED and the serving satellite can be obtained using the basic cosine theorem as

$$d(\varphi) = \sqrt{(R+H)^2 + R^2 - 2R(R+H) \cos \varphi}. \quad (8)$$

B. Channel Model

For the satellite-to-ground channel model within the underlying LoRa-based DtS-IoT system, we follow an empirically-verified model adopted in [43], [44], which leverages the recent developments in satellite-to-ground path-loss modeling and line-of-sight (LoS) probability formulation. As stated in [44], the radio signal travels mostly in free-space until it encounters the near-ground clutter layer where it interacts with both natural and artificial obstacles. These interactions include absorption, scattering, diffraction, and reflection, which leads to the excess path-loss. Therefore, both the free-space path loss and the excess path-loss are taken into account in our considered LoRa-based DtS-IoT system, which increases the applicability of the channel model in realistic scenarios.

Specifically, given the transmission distance $d(\varphi)$ and the carrier frequency f_c , the free-space path loss is given as

$$L(\varphi) = \left(\frac{c}{4\pi f_c d(\varphi)} \right)^2, \quad (9)$$

where c refers to the speed of light.

Moreover, let us denote η as the excess path-loss, which follows a mixed Gaussian distribution given as [44]

$$\begin{aligned} \eta [\text{dB}] &\sim p_{LoS}(\varphi) \mathcal{N}(-\mu_{LoS}, \sigma_{LoS}^2) + \\ &(1 - p_{LoS}(\varphi)) \mathcal{N}(-\mu_{NLoS}, \sigma_{NLoS}^2), \end{aligned} \quad (10)$$

where the parameters $\mu_{LoS}, \sigma_{LoS}, \mu_{NLoS}, \sigma_{NLoS}$ depend on the propagation environment and $p_{LoS}(\varphi)$ is the probability of LoS transmission, which can be calculated as [44]

$$p_{LoS}(\varphi) = \exp \left(-\frac{\beta \sin \varphi}{\cos \varphi - \alpha} \right), \quad (11)$$

where $\alpha = \frac{R}{R+H}$ and β depends on the propagation environment.

Notably, given the contact angle φ , the variations of the excess path-loss are considered to be negligible when compared to its mean value [45]. Accordingly, we use the average

¹The impact of varying number of interfering EDs on the system error performance is shown via numerical simulations.

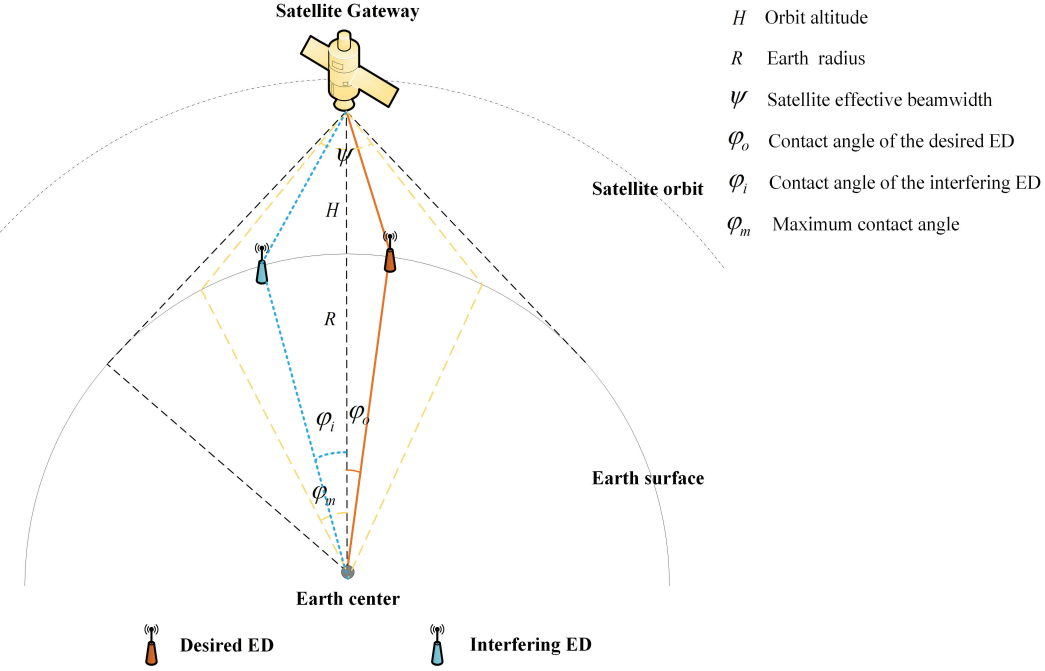


Fig. 1. An illustration of the network model of LoRa-based DtS-IoT, where the yellow dashed line represents the satellite footprint determined by the satellite effective beamwidth ψ while the black dashed line denotes the maximum satellite footprint corresponding to just covering the horizon.

excess path-loss $\bar{\eta}(\varphi)$ for the sake of simplicity, which can be expressed as [44]

$$\begin{aligned} \bar{\eta}(\varphi) = & p_{LoS}(\varphi) \exp\left(\frac{\zeta^2 \sigma_{LoS}^2}{2} - \zeta \mu_{LoS}\right) + \\ & (1 - p_{LoS}(\varphi)) \exp\left(\frac{\zeta^2 \sigma_{NLoS}^2}{2} - \zeta \mu_{NLoS}\right), \end{aligned} \quad (12)$$

where $\zeta \triangleq \frac{\ln(10)}{10}$.

C. Signal Model

As depicted in Fig. 1, φ_o and φ_i are the contact angles of the desired ED and interfering ED, respectively. Moreover, let P_o, G_o and P_i, G_i denote the transmit power and antenna gain of the desired ED and interfering ED, respectively. Then, the received signal at the satellite gateway can be expressed as

$$\begin{aligned} r_m[n] = & \underbrace{\sqrt{P_o G_o G_s L(\varphi_o)} \bar{\eta}(\varphi_o) s_m[n]}_{\text{desired signal}} + \underbrace{w[n]}_{\text{noise}} \\ & + \underbrace{\sqrt{P_i G_i G_s L(\varphi_i)} \bar{\eta}(\varphi_i) s_I[n] \exp\left\{j2\pi n \frac{\epsilon}{M}\right\}}_{\text{interfering signal}}, \end{aligned} \quad (13)$$

where G_s represents the satellite antenna gain, $s_m[n]$ and $s_I[n]$ are the transmitted LoRa signals of the desired ED and interfering ED, respectively, and ϵ denotes the normalized relative FO between them. Notably, the normalization is carried out with respect to $\Delta f = \frac{B}{M} = \frac{1}{T}$, where T is the symbol duration. Herein, we point out that both laboratory and flight testings have verified the strong immunity of LoRa-based LEO satellite communications to the Doppler effect [5], [6]. Namely, by availing of the effective synchronization algorithms employed in LoRa PHY layer [46], [47], the

H	Orbit altitude
R	Earth radius
ψ	Satellite effective beamwidth
φ_o	Contact angle of the desired ED
φ_i	Contact angle of the interfering ED
φ_m	Maximum contact angle

Doppler effect can be properly handled in LoRa-based DtS-IoT communications. Therefore, the onboard gateway can be assumed to be synchronized with the desired signal, which is a common assumption in many research works concerning interference-limited LoRa systems [25], [26], [37]. However, the relative frequency offset could appear between the desired and interfering signals due to the different frequency shifts experienced by them during the transmission. Also, the un-coordinated asynchronous transmission will inevitably lead to relative time offset between the desired and interfering signals.

More specifically, the relative FO can be decomposed into integer and fractional parts. Since the onboard gateway is assumed to be synchronized with the desired signal as stated before, the desired peak is fixed in the DFT output given a transmitted data symbol m . Thus, the relative FO will only impact the index and magnitude of the interference peak. As pointed out in [32], the integer FO simply leads to a cyclic shift of the peak index in the DFT output without energy spread. Therefore, only the fractional FO will impact the magnitude of the interference peak and thus the error performance. Consequently, we can only consider the impact of fractional FO, i.e., $\epsilon \in [0, 0.5]$, which causes the energy spread due to the limited DFT resolution. In particular, the time domain signal collision model is illustrated in Fig. 2, where the interfering signal is composed of two different LoRa symbols during each symbol period of the desired signal due to the asynchronous transmission. Without loss of generality, we assume that the relative time offset (TO) τ is an integer between 0 and $M - 1$, and thereby we have

$$s_I[n] = \begin{cases} s_{i_1}[n], & 0 \leq n < \tau, \\ s_{i_2}[n], & \tau \leq n < M - 1, \end{cases} \quad (14)$$

where $i_1, i_2 \in \mathcal{L}$ are the data symbols of the interfering signal.

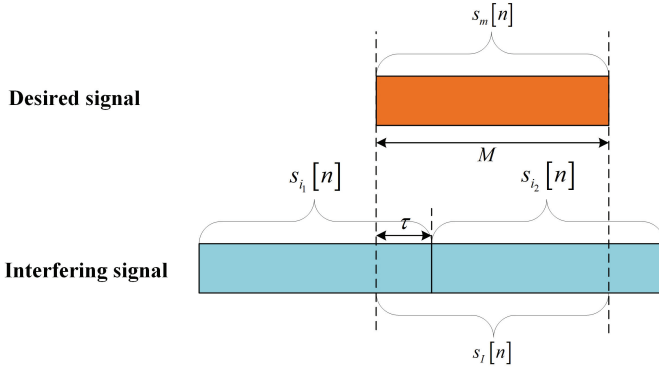


Fig. 2. An illustration of the time domain signal collision model.

IV. PROPOSED PERFORMANCE ANALYSIS

In this section, the theoretical error performance of LoRa-based DTS-IoT system is investigated. To this end, the decision metrics are first derived within the underlying system model.

A. Decision Metrics

As mentioned above, the detection for each LoRa symbol can be divided into dechirp, DFT, and FD peak index decision. Let $J_o = \sqrt{P_o G_o G_s L(\varphi_o) \bar{\eta}(\varphi_o)} M$ and $J_i = \sqrt{P_i G_i G_s L(\varphi_i) \bar{\eta}(\varphi_i)}$, the DFT output of the dechirped signal for a given m can be obtained as

$$R_m[l] = J_o \delta[l - m] + J_i \mathcal{I}[l] + W[l], \quad (15)$$

with

$$\begin{aligned} \mathcal{I}[l] &= \frac{\sin[\pi(i_1 - l + \epsilon)\tau/M]}{\sin[\pi(i_1 - l + \epsilon)/M]} \Phi_I + \\ &\quad \frac{\sin[\pi(i_2 - l + \epsilon)(M - \tau)/M]}{\sin[\pi(i_2 - l + \epsilon)/M]} \Phi_{II}, \end{aligned} \quad (16)$$

where $\Phi_I = \exp\{j\pi(i_1 - l + \epsilon)(\tau - 1)/M\}$, $\Phi_{II} = \exp\{j\pi(i_2 - l + \epsilon)(M + \tau - 1)/M\}$, and $\delta[\cdot]$ is the Kronecker delta function. A detailed derivation of (15) and (16) can be found in Appendix A.

Therefore, the received data symbol can be determined as

$$\hat{m} = \arg \max_{l \in \mathcal{L}} |J_o \delta[l - m] + J_i \mathcal{I}[l] + W[l]|, \quad (17)$$

for non-coherent detection.

B. Analytical Error Rate Expressions

According to (15), the decision metric $|R_m[l]|$ follows a Rician distribution with the Rician factor $\kappa_m = \frac{J_o^2 + J_i^2 |\mathcal{I}[m]|^2}{\sigma^2}$ for $l = m$ and $\kappa_l = \frac{J_i^2 |\mathcal{I}[l]|^2}{\sigma^2}$ for $l \neq m$. For $l = m$, $|R_m[l]|$ can be approximated by a Gaussian random variable with mean $J_o + J_i |\mathcal{I}[m]|$ and variance $\frac{\sigma^2}{2}$. For $l \neq m$, the frequency bins of the DFT output can be divided into two sets, namely, interference-driven set $S_I = \{\kappa_l \geq \Xi, l \neq m\}$ and noise-driven set $S_N = \{\kappa_l < \Xi, l \neq m\}$, based on the value of κ_l , where Ξ is an empirical predefined threshold [32]. More specifically, for $l \in S_I$, $|R_m[l]|$ can be approximated by a Gaussian random variable with mean $J_i |\mathcal{I}[l]|$ and variance

$\frac{\sigma^2}{2}$, while for $l \in S_N$, $|R_m[l]|$ can be approximated by a Rayleigh random variable.

Let us denote $\rho = \max_{l \in S_N} |R_m[l]|$ and to obtain the statistical properties of ρ , we first introduce the following proposition.

Proposition 1. We define $H_N = \sum_{i=1}^N \frac{1}{i}$ as the N -th harmonic number and $H_N^{(2)} = \sum_{i=1}^N \frac{1}{i^2}$. Thus, we have

$$\sum_{k=1}^N (-1)^{k-1} \frac{1}{k} \binom{N}{k} = H_N, \quad (18)$$

$$2 \sum_{k=1}^N (-1)^{k-1} \frac{1}{k^2} \binom{N}{k} = H_N^2 + H_N^{(2)}, \quad (19)$$

where $H_N^{(2)}$ will converge to $\frac{\pi^2}{6}$ for a sufficiently large N .

Proof: See Appendix B. ■

Based on this, we have the following proposition.

Proposition 2. Using a moment matching method, ρ can be approximated by a Gaussian random variable with mean

$$\mu_\rho = \sigma \left(H_{|S_N|}^2 - \frac{H_{|S_N|}^{(2)}}{2} \right)^{\frac{1}{4}}, \quad (20)$$

and variance

$$\sigma_\rho^2 = \sigma^2 \left(H_{|S_N|}^2 - \sqrt{H_{|S_N|}^2 - \frac{H_{|S_N|}^{(2)}}{2}} \right). \quad (21)$$

Proof: See Appendix C. ■

In addition, we approximate the impact of the overall interference distributed within the decision metrics by that of the peak interference appearing at a certain frequency bin to simplify the analysis. Specifically, we assume that the interfering term $\mathcal{I}[l]$ exhibits a peak magnitude at a certain frequency bin $\tilde{m} \neq m$ for each realization of i_1 , i_2 , m , and τ , while its magnitudes over the remaining frequency bins can be negligible. Given that $k \geq 7$ and thus $M \geq 128$, the peak interference is most likely to appear on a different frequency bin from that of the desired signal. Accordingly, we can only consider the case of $\tilde{m} \neq m$ to analyze the error performance of LoRa-based DTS-IoT system. The accuracy of this approximation will be shown in Section V through numerical simulations. Regarding the peak magnitude of the interfering term, we have the following proposition.

Proposition 3. The upper bound for the magnitude of the interfering term $\mathcal{I}[l]$ can be obtained as

$$|\mathcal{I}[l]| \leq \Lambda_{\chi, \tau} = \left| \frac{\sin(\pi \chi \tau / M)}{\sin(\pi \chi / M)} \right| + M - \tau, \quad (22)$$

where χ is uniformly distributed in \mathcal{L} and τ is an integer uniformly distributed within $[0, \frac{M}{2}]$.

Proof: See Appendix D. ■

Hence, the DFT output of (15) becomes

$$R_{m,\tilde{m}}[l] = \begin{cases} J_o + W[m], & l = m, \\ J_i \Lambda_{\chi,\tau} + W[\tilde{m}], & l = \tilde{m}, \\ W[l], & l \neq m, \tilde{m}. \end{cases} \quad (23)$$

Therefore, the approximate SER can be divided into noise-driven SER, \tilde{P}_s^N , and interference-driven SER, \tilde{P}_s^I , respectively. On one hand, the noise-driven SER, \tilde{P}_s^N , can be obtained as

$$\begin{aligned} \tilde{P}_s^N &= \mathbb{P} \left\{ \max_{l \neq m, \tilde{m}} |W[l]| > |J_o + W[m]| \right\} \\ &\stackrel{(a)}{\approx} Q \left(\frac{J_o - \sigma \left(H_{M-2}^2 - \frac{\pi^2}{12} \right)^{\frac{1}{4}}}{\sqrt{\frac{\sigma^2}{2} + \sigma^2 \left(H_{M-2}^2 - \sqrt{H_{M-2}^2 - \frac{\pi^2}{12}} \right)}} \right). \end{aligned} \quad (24)$$

where step (a) follows that $|S_N| = M - 2 \gg 1$.

On the other hand, the conditional interference-driven SER can be obtained as

$$\begin{aligned} \tilde{P}_s^{I|\chi,\tau} &= \mathbb{P} \left\{ |J_i \Lambda_{\chi,\tau} + W[\tilde{m}]| > |J_o + W[m]| \right\} \\ &\approx Q \left(\frac{J_o - J_i \Lambda_{\chi,\tau}}{\sigma} \right). \end{aligned} \quad (25)$$

Given that χ and τ are uniformly distributed between 0 and $M - 1$ as well as 0 and $\frac{M}{2} - 1$, the approximate interference-driven SER, \tilde{P}_s^I , can be computed as

$$\begin{aligned} \tilde{P}_s^I &= \frac{1}{M \left(\frac{M}{2} \right)} \sum_{\chi=0}^{M-1} \sum_{\tau=0}^{\frac{M}{2}-1} \tilde{P}_s^{I|\chi,\tau} \\ &\approx \frac{2}{M^2} \sum_{\chi=0}^{M-1} \sum_{\tau=0}^{\frac{M}{2}-1} Q \left(\frac{J_o - J_i \Lambda_{\chi,\tau}}{\sigma} \right). \end{aligned} \quad (26)$$

Since the noise-driven SER, \tilde{P}_s^N , and interference-driven SER, \tilde{P}_s^I , are independent, the closed-form BER can be obtained by combining (24) and (26) as

$$\tilde{P}_b = \frac{M}{2(M-1)} \left[1 - \left(1 - \tilde{P}_s^N \right) \left(1 - \tilde{P}_s^I \right) \right]. \quad (27)$$

From (27), one can observe that both the noise-driven SER, \tilde{P}_s^N , and interference-driven SER, \tilde{P}_s^I , play a dominant role in determining the overall error performance of our considered LoRa-based DtS-IoT system. This indicates that the error performance can be improved by increasing the received signal-to-noise ratio (SNR) of the desired ED via proper link budget and/or increasing the received SIR of the desired ED through controlling the satellite effective beamwidth, i.e., reducing the aggregated interference. Moreover, when the interfering ED is outside the satellite effective beamwidth, no interference-driven error occurs, which represents an ideal interference-free

TABLE II
SIMULATION PARAMETERS

Notation	Values
Earth radius R	6371 km
Orbit altitude H	500 km
Satellite effective beamwidth ψ	50°
Carrier frequency f_c	868 MHz
Bandwidth B	125 kHz
Spreading factor k	7, 8, 9
Fractional FO ϵ	0.1
Transmit power of interfering ED P_i	14 dBm
Noise figure N_F	6 dB
Satellite antenna gain G_s	10 dBi
ED's antenna gain G_o, G_i	2.15 dBi
Contact angle of interfering ED φ_i	0°
LoS probability parameter β	2.3
LoS mean EPL μ_{LoS}	0 dB
LoS EPL standard deviation σ_{LoS}	2.8 dB
NLoS mean EPL μ_{NLoS}	12 dB
NLoS EPL standard deviation σ_{NLoS}	9 dB

scenario, and thus the approximate BER becomes²

$$\begin{aligned} \tilde{P}_b^* &\approx \frac{M}{2(M-1)} \times \\ &Q \left(\frac{J_o - \sigma \left(H_{M-1}^2 - \frac{\pi^2}{12} \right)^{\frac{1}{4}}}{\sqrt{\frac{\sigma^2}{2} + \sigma^2 \left(H_{M-1}^2 - \sqrt{H_{M-1}^2 - \frac{\pi^2}{12}} \right)}} \right), \end{aligned} \quad (28)$$

which will go to zero with the increase of P_o since $J_o = \sqrt{P_o G_o G_s L(\varphi_o) \bar{\eta}(\varphi_o)} M$.

V. NUMERICAL PERFORMANCE EVALUATION

In this section, we validate our theoretical performance analysis through Monte-Carlo simulations under practical system parameters, which also provides valuable insights into the error performance improvements of our considered LoRa-based DtS-IoT system. Unless otherwise specified, the parameter values used in our simulations are summarized in Table II, where the majority of these parameters are in accordance with [25], [32], [37], [43], [44].

First, Figs. 3(a) and 3(b) show that the impact of the overall interference distributed within the decision metrics can be approximated by that of the peak interference appearing at a certain frequency bin, where N_i denotes the number of interfering EDs. For $N_i = 1$ (i.e., relatively sparse deployment), a specific example for $\tau = 105$, $i_1 = 34$, and $i_2 = 62$ is shown in Fig. 3(a). It can be observed that the overall interference distributed within the decision metrics, i.e., $|\mathcal{I}[l]|$, exhibits a peak magnitude at a certain frequency bin $\tilde{m} \neq m$ while its magnitudes over the remaining frequency bins can be approximately negligible. Since the onboard gateway is assumed to

²Note that $|S_N| = M - 1$ in the absence of interference.

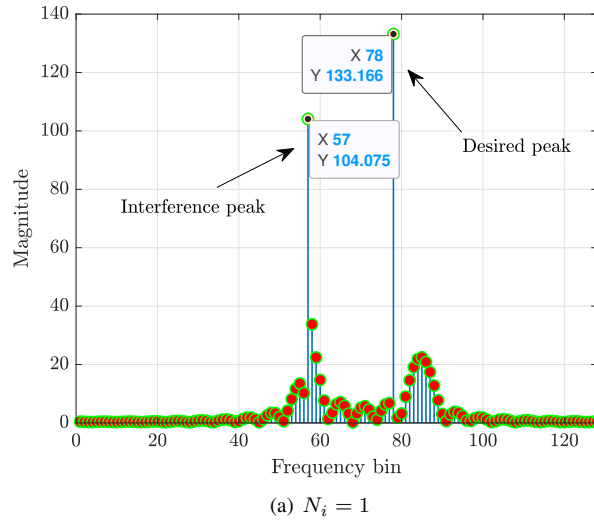
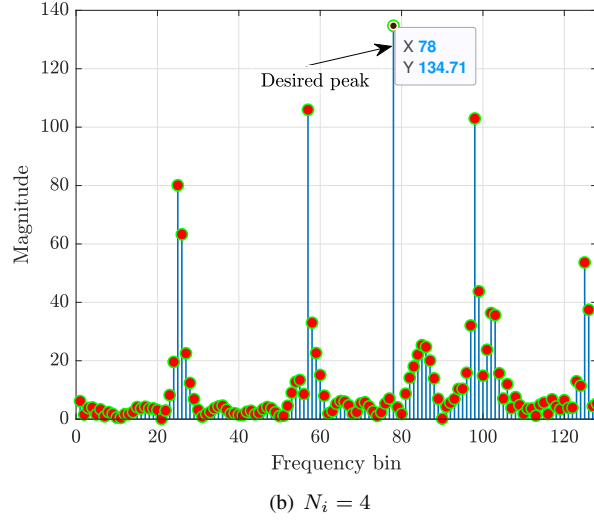
(a) $N_i = 1$ (b) $N_i = 4$

Fig. 3. DFT output for $P_o = 14$ dBm, $\varphi_o = 0^\circ$, SF = 7, and $m = 78$ with the number of interfering EDs: (a) $N_i = 1$ and (b) $N_i = 4$.

be synchronized with the desired signal, the position of the desired peak is fixed in the DFT output given a transmitted data symbol m , as illustrated in Fig. 3(a). However, due to the uncoordinated asynchronous transmission, relative time and frequency offset appear in the interfering signal, which could change the position of the interference peaks and thus no direct relationship between the position of the interference peaks and the given values of the interfering symbols exists. Nevertheless, we have proved that $|\mathcal{I}[l]| \leq \Lambda_{\chi,\tau}$ in Proposition 3, which validates the effectiveness of our subsequent error performance analysis. Furthermore, for $N_i = 4$ (i.e., relatively dense deployment), more interference peaks appear in the DFT output as illustrated in Fig. 3(b) while the error margin of the approximation can be amplified, which may lead to an error performance degradation in such scenarios.

Herein, Figs. 4(a) and 4(b) demonstrate the BER performance versus P_o for $B = 125$ kHz and $B = 250$ kHz, respectively. It can be observed that the numerical results

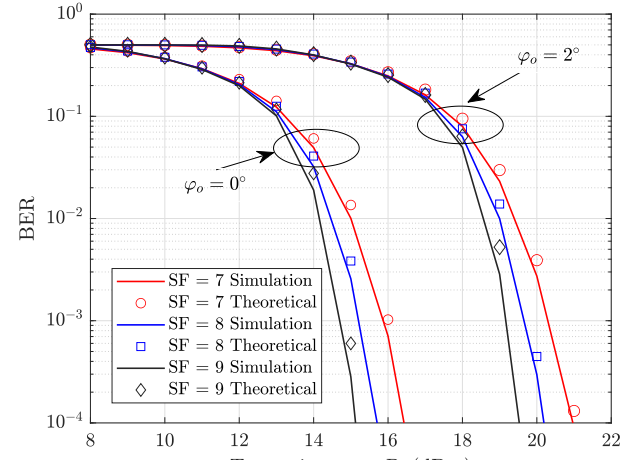
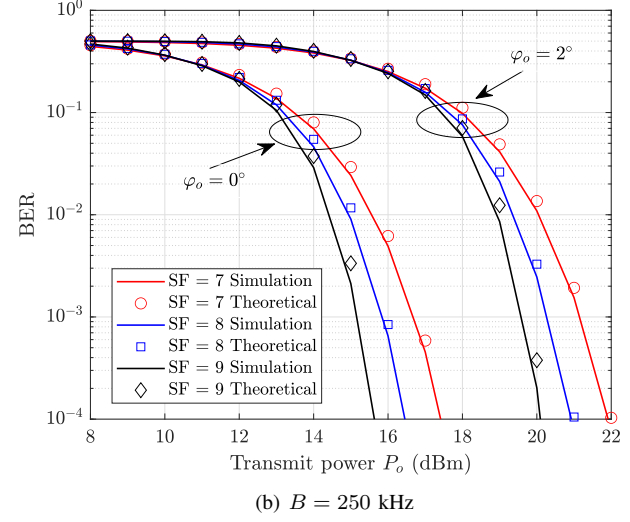
(a) $B = 125$ kHz(b) $B = 250$ kHz

Fig. 4. BER performance versus P_o for (a) $B = 125$ kHz and (b) $B = 250$ kHz.

match well with the analytical results, which substantiate our theoretical analysis. From the figures, it can be seen that the BER performance of the underlying LoRa-based DtS-IoT system improves with the increase of SF due to the larger spreading gain of CSS modulation. It can be further noticed that the contact angle of the desired ED, i.e., ED's location, has remarkable impact on the system error performance. This is due to the fact that as φ_o increases, the desired signal quality decreases due to the amplified satellite-to-ground path-loss while the impact of interfering signal becomes more dominant, and thus leading to a serious performance deterioration. Moreover, by comparing Figs. 4(a) and 4(b), one can observe that a narrower bandwidth leads to a better BER performance of the underlying system since the noise power is determined by the signal bandwidth, quantified as $\sigma_q^2 = -174 + N_F + 10 \log_{10} B$ with N_F representing the receiver's noise figure.

Furthermore, to illustrate the link-level performance of the underlying LoRa-based DtS-IoT system more intuitively, Figs.

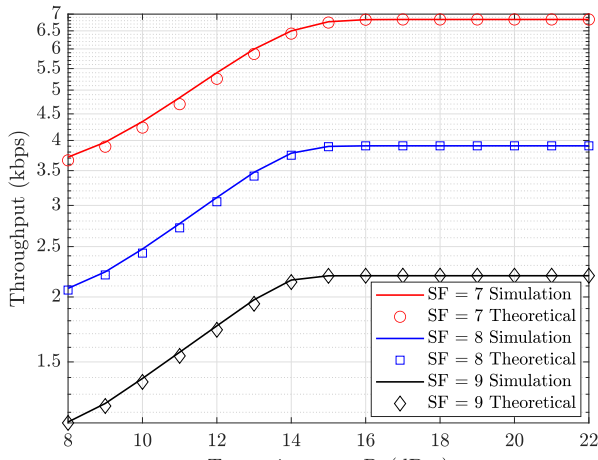
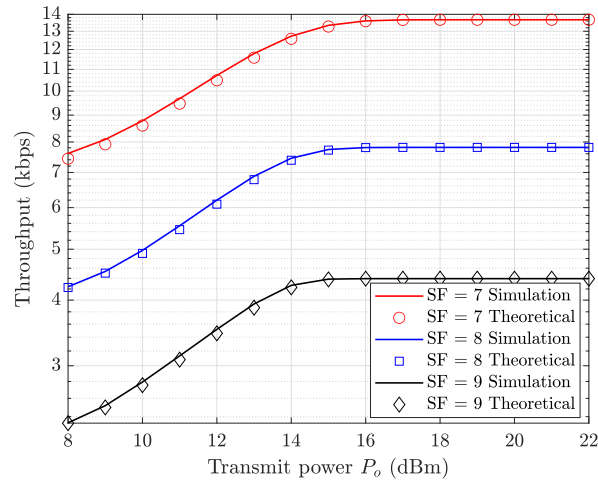
(a) $B = 125 \text{ kHz}$ (b) $B = 250 \text{ kHz}$

Fig. 5. Effective throughput versus P_o for (a) $B = 125 \text{ kHz}$ and (b) $B = 250 \text{ kHz}$.

5(a) and 5(b) depict the effective throughput versus P_o for $B = 125 \text{ kHz}$ and $B = 250 \text{ kHz}$, respectively. In particular, the effective throughput T_E (bps) can be defined as [40]

$$T_E = \eta B(1 - P_b), \quad (29)$$

where P_b denotes the BER and $\eta = \frac{k}{2^k}$ represents the spectral efficiency of LoRa modulation. By inspecting Fig. 4 and Fig. 5, it can be observed that increasing the SF and/or decreasing the bandwidth will significantly reduce the effective throughput while improving the BER performance, which presents a compelling trade-off between the error performance and the achievable data rate within our considered LoRa-based DtS-IoT system. This indicates that the underlying LoRa-based DtS-IoT system supports flexible adaptive transmission by adjusting the configurable SF and bandwidth parameters according to the practical application scenarios and different quality of service (QoS) requirements.

Figs. 6(a) and 6(b) present the numerical BER of our

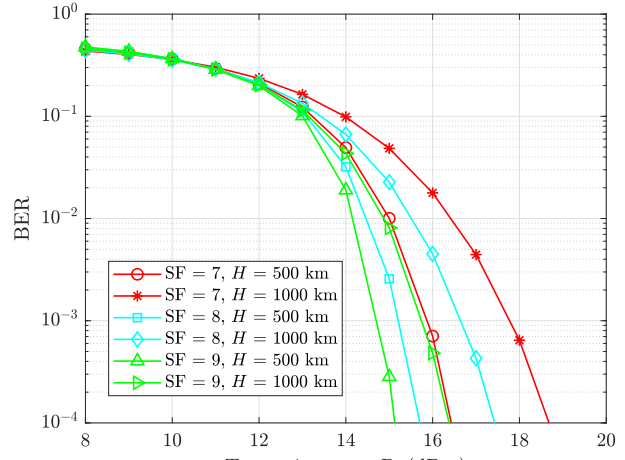
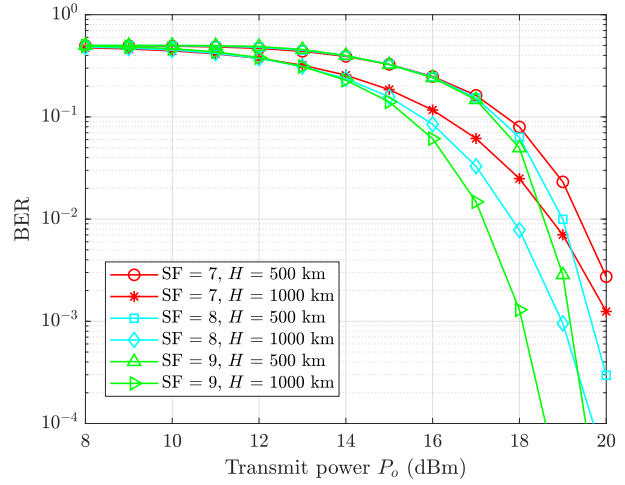
(a) $\varphi_o = 0^\circ$ (b) $\varphi_o = 2^\circ$

Fig. 6. Numerical BER versus P_o with different orbit altitudes for (a) $\varphi_o = 0^\circ$ and (b) $\varphi_o = 2^\circ$ with $B = 125 \text{ kHz}$.

considered LoRa-based DtS-IoT system with different orbit altitudes for $\varphi_o = 0^\circ$ and $\varphi_o = 2^\circ$, respectively. The obtained results further demonstrate the advantage of LoRa-based DtS-IoT communications. In particular, although the system performance is severely affected by the satellite orbit altitude, it can be noticed that the underlying system experiences acceptable BER performance for all SFs even at $H = 1000 \text{ km}$, which characterizes highly reliable energy-efficient communication links. This further motivates us to exploit LoRa-based DtS-IoT systems as a green and cost-effective approach for ubiquitous IoT connectivity.

Figs. 7(a) and 7(b) compare the BER performance of LoRa-based DtS-IoT system with and without interference for $B = 125 \text{ kHz}$ and $B = 250 \text{ kHz}$, respectively, with $H = 500 \text{ km}$ and $\varphi_o = 2^\circ$. In particular, since the orbit altitude is $H = 500 \text{ km}$ and the satellite effective beamwidth is $\psi = 50^\circ = \frac{5}{18}\pi \approx 0.8727$, we have $\psi_0 = 2\sin^{-1}\left(\frac{R}{R+H}\right) \approx 2.3739 > \psi$ in this case. Accordingly, the maximum contact angle can be deter-

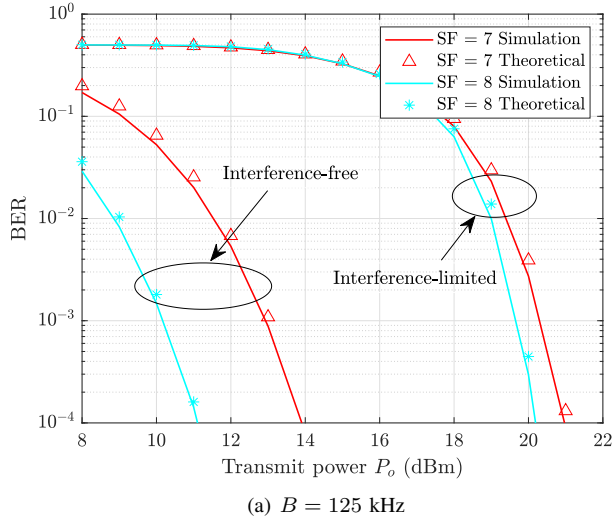
(a) $B = 125 \text{ kHz}$ (b) $B = 250 \text{ kHz}$

Fig. 7. BER performance versus P_o with and without interference for (a) $B = 125 \text{ kHz}$ and (b) $B = 250 \text{ kHz}$ with $H = 500 \text{ km}$ and $\varphi_o = 2^\circ$.

mined according to (7) as $\varphi_m = \sin^{-1} \left(\frac{R+H}{R} \sin \left(\frac{\psi}{2} \right) \right) - \frac{\psi}{2} \approx 0.0369 = 2.1155^\circ$. Therefore, we set the contact angle of the desired ED as $\varphi_o = 2^\circ$, which is within the satellite footprint while approaching the coverage border. The simulation results in the interference-free scenarios also agree well with the theoretical results, which verifies the correctness of our analysis once again and provides an upper bound for the practical BER performance in interference-limited scenarios. Moreover, the BER performance gap between two adjacent SFs in interference-free scenarios is larger than that of the interference-limited scenarios. It can also be observed that the underlying system is very sensitive to the interference, where a severe performance degradation appears in interference-limited scenarios when compared to interference-free scenarios. For example, when $B = 125 \text{ kHz}$, the performance loss is around 7 dB and 9 dB for SF = 7 and SF = 8 at the BER level of 10^{-4} , respectively, which leads to an increased energy consumption for resource-limited LoRa EDs. Moreover, it can

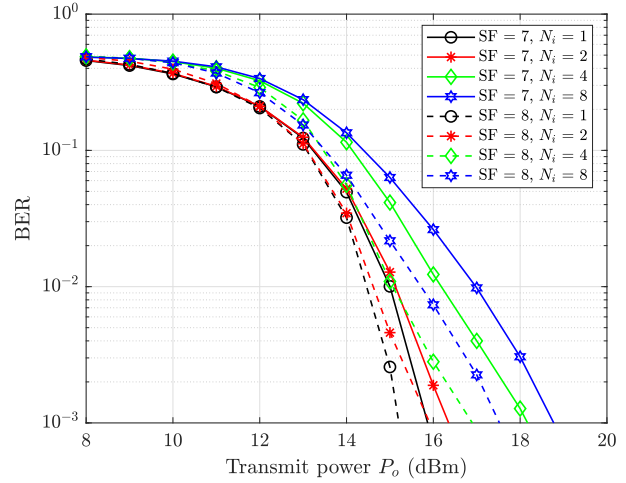


Fig. 8. BER performance versus P_o with varying number of interfering EDs N_i for SF = 7 and SF = 8.

be expected that a more detrimental impact on the system error performance will appear when the effect of the interfering signal becomes more dominant. Herein, Fig. 8 demonstrates the BER performance of our considered LoRa-based DtS-IoT system with varying number of interfering EDs for SF = 7 and SF = 8. It can be observed that the system error performance degrades with the increase of N_i , which could lead to a serious energy efficiency loss for low-power and long-range communications through such a new paradigm. Consequently, it is of great significance to conceive interference suppression techniques for our considered LoRa-based DtS-IoT system.

As such, based on our analysis and the above numerical results, we outline the following future research directions for improving the error performance of LoRa-based DtS-IoT system from the PHY layer perspective:

- On one hand, the error performance of LoRa-based DtS-IoT system can be improved by developing advanced forward error correction (FEC) strategies. In particular, although Hamming code is currently adopted in LoRa PHY layer, more advanced channel coding schemes can be utilized to further enhance the error performance of LoRa-based communication system. For example, Turbo codes [48] and low-density parity-check (LDPC) codes [49] have been investigated as potential approaches for further improving the BER performance of LoRa modulation. It has been shown that a proper channel coding scheme could lead to a more extensive trade-off between energy and spectral efficiency. This motivates a more in-depth study into the appropriate channel coding schemes for LoRa-based DtS-IoT systems.
- On the other hand, the error performance of LoRa-based DtS-IoT system can be further enhanced by leveraging more advanced signal detection methods. Specifically, deep learning (DL) based techniques, like deep neural networks (DNNs) and convolutional neural networks (CNNs), have been proven to be a more effective approach for signal detection of LoRa-based communication system in interference-limited scenarios compared

to the conventional coherent and non-coherent detection [50], [51], which remains an interesting topic for future research.

VI. CONCLUSION

In this paper, a novel analytical framework for characterizing the error performance of LoRa-based DtS-IoT system has been developed by leveraging an empirically-verified satellite-to-ground channel model. To enable a realistic performance analysis, non-coherent detection is considered in the presence of interference along with the relative time and frequency offsets, where the corresponding decision metrics are analytically derived. Based on this, closed-form symbol and bit error rate expressions are derived by using a moment matching method and approximating the impact of the overall interference distributed within the decision metrics by that of the peak interference. Moreover, the impact of some key system parameters, such as the SF, the bandwidth, the ED's location, and the varying number of interfering EDs, on the error performance of our considered LoRa-based DtS-IoT system is thoroughly investigated. Numerical simulations not only validate the accuracy of our theoretical analysis but also provide further insights into the error performance improvements of such a new paradigm. Overall, we believe that our work will set a solid foundation for LoRa-based DtS-IoT system which serves as a promising solution for low-power, long-range, and ubiquitous IoT applications.

APPENDIX A DERIVATION OF (15) AND (16)

According to (4), (13), and (14), we have

$$\begin{aligned} R_m[l] &= \sum_{n=0}^{M-1} r_m[n] u^*[n] \exp \left\{ -j \frac{2\pi ln}{M} \right\} \\ &= \frac{1}{M} \sum_{n=0}^{M-1} J_o s_m[n] u^*[n] \exp \left\{ -j \frac{2\pi ln}{M} \right\} \\ &\quad + \sum_{n=0}^{M-1} J_i s_I[n] u^*[n] \exp \left\{ j \frac{2\pi \epsilon n}{M} \right\} \exp \left\{ -j \frac{2\pi ln}{M} \right\} \\ &\quad + \sum_{n=0}^{M-1} w[n] u^*[n] \exp \left\{ -j \frac{2\pi ln}{M} \right\} \\ &= J_o \delta[l-m] + J_i \mathcal{I}[l] + W[l], \end{aligned} \quad (30)$$

with

$$\begin{aligned} \mathcal{I}[l] &= \sum_{n=0}^{M-1} s_I[n] u^*[n] \exp \left\{ j \frac{2\pi \epsilon n}{M} \right\} \exp \left\{ -j \frac{2\pi ln}{M} \right\} \\ &= \sum_{n=0}^{\tau-1} s_{i_1}[n] u^*[n] \exp \left\{ j \frac{2\pi \epsilon n}{M} \right\} \exp \left\{ -j \frac{2\pi ln}{M} \right\} \\ &\quad + \sum_{n=\tau}^{M-1} s_{i_2}[n] u^*[n] \exp \left\{ j \frac{2\pi \epsilon n}{M} \right\} \exp \left\{ -j \frac{2\pi ln}{M} \right\} \\ &= \sum_{n=0}^{\tau-1} \exp \left\{ j \frac{2\pi n(i_1 - l + \epsilon)}{M} \right\} + \sum_{n=\tau}^{M-1} \exp \left\{ j \frac{2\pi n(i_2 - l + \epsilon)}{M} \right\} \\ &\stackrel{(a)}{=} \frac{1 - \exp \left\{ j \frac{2\pi \tau(i_1 - l + \epsilon)}{M} \right\}}{1 - \exp \left\{ j \frac{2\pi(i_1 - l + \epsilon)}{M} \right\}} \\ &\quad + \exp \left\{ j \frac{2\pi \tau(i_2 - l + \epsilon)}{M} \right\} \frac{1 - \exp \left\{ j \frac{2\pi(M-\tau)(i_2 - l + \epsilon)}{M} \right\}}{1 - \exp \left\{ j \frac{2\pi(i_2 - l + \epsilon)}{M} \right\}} \\ &= \exp \left\{ j \frac{\pi(\tau-1)(i_1 - l + \epsilon)}{M} \right\} \times \\ &\quad \frac{\exp \left\{ -j \frac{\pi \tau(i_1 - l + \epsilon)}{M} \right\} - \exp \left\{ j \frac{\pi \tau(i_1 - l + \epsilon)}{M} \right\}}{\exp \left\{ -j \frac{\pi(i_1 - l + \epsilon)}{M} \right\} - \exp \left\{ j \frac{\pi(i_1 - l + \epsilon)}{M} \right\}} \\ &\quad + \exp \left\{ j \frac{\pi(M+\tau-1)(i_2 - l + \epsilon)}{M} \right\} \times \\ &\quad \frac{\exp \left\{ -j \frac{\pi(M-\tau)(i_2 - l + \epsilon)}{M} \right\} - \exp \left\{ j \frac{\pi(M-\tau)(i_2 - l + \epsilon)}{M} \right\}}{\exp \left\{ -j \frac{\pi(i_2 - l + \epsilon)}{M} \right\} - \exp \left\{ j \frac{\pi(i_2 - l + \epsilon)}{M} \right\}} \\ &= \frac{\sin[\pi(i_1 - l + \epsilon)\tau/M]}{\sin[\pi(i_1 - l + \epsilon)/M]} \Phi_I + \\ &\quad \frac{\sin[\pi(i_2 - l + \epsilon)(M-\tau)/M]}{\sin[\pi(i_2 - l + \epsilon)/M]} \Phi_{II}, \end{aligned} \quad (31)$$

where step (a) follows from the geometric series summation, $\Phi_I = \exp\{j\pi(i_1 - l + \epsilon)(\tau - 1)/M\}$, and $\Phi_{II} = \exp\{j\pi(i_2 - l + \epsilon)(M + \tau - 1)/M\}$.

APPENDIX B PROOF OF PROPOSITION 1

Let $\Theta_N = \sum_{k=1}^N (-1)^{k-1} \frac{1}{k} \binom{N}{k}$, we have

$$\begin{aligned} \Theta_N &\stackrel{(a)}{=} \int_0^1 \sum_{k=1}^N (-1)^{k-1} \binom{N}{k} x^{k-1} dx \\ &\stackrel{(b)}{=} \int_0^1 \frac{1 - (1-x)^N}{x} dx \\ &\stackrel{(c)}{=} \int_0^1 (1+t+\dots+t^{N-1}) dt \\ &= 1 + \frac{1}{2} + \dots + \frac{1}{N} = H_N, \end{aligned} \quad (32)$$

where step (a) follows the simple integral identity $\int_0^1 x^{k-1} dx = \frac{1}{k}$, step (b) follows the Newton's binomial theorem [52], and step (c) follows $t = 1 - x$.

Moreover, let $u(x) = \sum_{k=1}^N (-1)^{k-1} \frac{1}{k^2} \binom{N}{k} x^k$. Then, we have

$$u'(x) = \frac{du(x)}{dx} = \sum_{k=1}^N \frac{1}{k} \binom{N}{k} (-x)^{k-1}. \quad (33)$$

Let $w(x) = -xu'(x)$, we have

$$w'(x) = \frac{dw(x)}{dx} = -\sum_{k=1}^N \binom{N}{k} (-x)^{k-1} = \frac{(1-x)^N - 1}{x}. \quad (34)$$

As such, $w(x)$ can be expressed as

$$\begin{aligned} w(x) &= \int_0^x \frac{(1-y)^N - 1}{y} dy \\ &\stackrel{(a)}{=} \int_1^{1-x} (1+t+\dots+t^{N-1}) dt \\ &\stackrel{(b)}{=} -x + \frac{1}{2} \sum_{k=1}^2 (-1)^k \binom{2}{k} x^k + \dots \\ &\quad + \frac{1}{N} \sum_{k=1}^N (-1)^k \binom{N}{k} x^k, \end{aligned} \quad (35)$$

where step (a) follows $t = 1 - y$ and step (b) leverages the Newton's binomial theorem [52].

As a result, we have

$$\begin{aligned} u'(x) &= -\frac{w(x)}{x} \\ &= 1 + \frac{1}{2} \sum_{k=1}^2 (-1)^{k-1} \binom{2}{k} x^{k-1} + \dots \\ &\quad + \frac{1}{N} \sum_{k=1}^N (-1)^{k-1} \binom{N}{k} x^{k-1}, \end{aligned} \quad (36)$$

and thereby

$$\begin{aligned} u(1) &= \int_0^1 u'(x) dx \\ &= 1 + \frac{1}{2} \sum_{k=1}^2 (-1)^{k-1} \frac{1}{k} \binom{2}{k} + \dots \\ &\quad + \frac{1}{N} \sum_{k=1}^N (-1)^{k-1} \frac{1}{k} \binom{N}{k}. \end{aligned} \quad (37)$$

Recalling that $u(x) = \sum_{k=1}^N (-1)^{k-1} \frac{1}{k^2} \binom{N}{k} x^k$ and $\Theta_N = \sum_{k=1}^N (-1)^{k-1} \frac{1}{k} \binom{N}{k} = H_N$, we have

$$2u(1) = 2 \sum_{k=1}^N (-1)^{k-1} \frac{1}{k^2} \binom{N}{k} = H_N^2 + H_N^{(2)}, \quad (38)$$

where $H_N^{(2)} = \sum_{i=1}^N \frac{1}{i^2}$. The proof is completed.

APPENDIX C PROOF OF PROPOSITION 2

Herein, we use a moment-matching method to fit the random variable $\rho = \max_{l \in S_N} |R_m[l]|$ to the Gaussian distribution, i.e., $\rho \sim \mathcal{N}(\mu_\rho, \sigma_\rho^2)$. As such, the n -th moment of ρ can be

derived from the n -th differential of the moment generating function (MGF) $M_\rho[t] = \exp(\mu_\rho t + \frac{1}{2}\sigma_\rho^2 t^2)$ evaluated at $t = 0$. In particular, the second and fourth moments of ρ can be obtained as

$$\mathbb{E}[\rho^2] = \frac{d^2 M_\rho[t]}{dt^2} \Big|_{t=0} = \mu_\rho^2 + \sigma_\rho^2, \quad (39)$$

$$\mathbb{E}[\rho^4] = \frac{d^4 M_\rho[t]}{dt^4} \Big|_{t=0} = \mu_\rho^4 + 6\mu_\rho^2\sigma_\rho^2 + 3\sigma_\rho^4. \quad (40)$$

To obtain μ_ρ and σ_ρ^2 , let us denote $\rho_l = |R_m[l]|, l \in S_N$, which follows a Rayleigh distribution and $\gamma_l = \rho_l^2$ which follows Chi-square distribution with one degree of freedom (i.e., exponential distribution). The CDF of γ_l is given by

$$F_{\gamma_l}(x) = 1 - \exp\left(-\frac{x}{\sigma^2}\right), \quad (41)$$

where $\sigma^2 = M\sigma_q^2$ with σ_q^2 denoting the variance of the received AWGN sample as expressed in (13). Let us define $\gamma = \max_{l \in S_N} \gamma_l$ which corresponds to the maximum of $|S_N|$ independent and identically distributed (i.i.d) exponential random variables, and its CDF and PDF can be calculated as

$$F_\gamma(x) = \mathbb{P}\left\{\max_{l \in S_N} \gamma_l \leq x\right\} = \left[1 - \exp\left(-\frac{x}{\sigma^2}\right)\right]^{|S_N|}, \quad (42)$$

$$\begin{aligned} f_\gamma(x) &= \frac{d}{dx} \left[1 - \exp\left(-\frac{x}{\sigma^2}\right)\right]^{|S_N|} \\ &= \frac{|S_N|}{\sigma^2} \exp\left(-\frac{x}{\sigma^2}\right) \left[1 - \exp\left(-\frac{x}{\sigma^2}\right)\right]^{|S_N|-1} \\ &\stackrel{(a)}{=} \sum_{k=0}^{|S_N|-1} |S_N| \binom{|S_N|-1}{k} \frac{(-1)^k}{\sigma^2} \exp\left(-\frac{(k+1)x}{\sigma^2}\right), \end{aligned} \quad (43)$$

where step (a) leverages the Newton's binomial theorem [52].

Let us denote μ_γ and σ_γ^2 as the mean and variance of γ , respectively, and using the moment matching method, we have

$$\mathbb{E}[\gamma] = \mu_\gamma = \mathbb{E}[\rho^2] = \mu_\rho^2 + \sigma_\rho^2, \quad (44)$$

$$\mathbb{E}[\gamma^2] = \mu_\gamma^2 + \sigma_\gamma^2 = \mathbb{E}[\rho^4] = \mu_\rho^4 + 6\mu_\rho^2\sigma_\rho^2 + 3\sigma_\rho^4. \quad (45)$$

Consequently, μ_ρ and σ_ρ^2 can be obtained as

$$\mu_\rho = \left(\mu_\gamma^2 - \frac{\sigma_\gamma^2}{2}\right)^{\frac{1}{4}}, \quad (46)$$

$$\sigma_\rho^2 = \mu_\gamma - \sqrt{\mu_\gamma^2 - \frac{\sigma_\gamma^2}{2}}, \quad (47)$$

with

$$\begin{aligned} \mu_\gamma &= \mathbb{E}[\gamma] \stackrel{(a)}{=} \int_0^\infty \sum_{k=1}^{|S_N|} \binom{|S_N|}{k} \frac{(-1)^{k-1} k x}{\sigma^2} \exp\left(-\frac{k x}{\sigma^2}\right) dx \\ &= \sigma^2 \sum_{k=1}^{|S_N|} (-1)^{k-1} \frac{1}{k} \binom{|S_N|}{k}, \end{aligned} \quad (48)$$

where step (a) follows that $|S_N| \binom{|S_N|-1}{k} = (k+1) \binom{|S_N|}{k+1}$

1
2
and

$$\sigma_{\gamma}^2 = \mathbb{E} [\gamma^2] - \mu_{\gamma}^2 = 2\sigma^4 \sum_{k=1}^{|S_N|} (-1)^{k-1} \frac{1}{k^2} \binom{|S_N|}{k} - \mu_{\gamma}^2. \quad (49)$$

3
4
5
6
7 Leveraging (18) and (19) in Proposition 1, μ_{γ} and σ_{γ}^2 can
8 be further simplified as

$$\mu_{\gamma} = \sigma^2 H_{|S_N|}, \quad (50)$$

$$\sigma_{\gamma}^2 = \sigma^4 H_{|S_N|}^{(2)}. \quad (51)$$

9
10 By substituting (50) and (51) into (46) and (47), μ_{ρ} and σ_{ρ}^2
11 can be obtained as

$$\mu_{\rho} = \sigma \left(H_{|S_N|}^2 - \frac{H_{|S_N|}^{(2)}}{2} \right)^{\frac{1}{4}}, \quad (52)$$

$$\sigma_{\rho}^2 = \sigma^2 \left(H_{|S_N|} - \sqrt{H_{|S_N|}^2 - \frac{H_{|S_N|}^{(2)}}{2}} \right). \quad (53)$$

12
13
14 The proof is completed.

APPENDIX D PROOF OF PROPOSITION 3

15 An upper bound of $|\mathcal{I}[l]|$ can be obtained by applying the
16 absolute value inequality to (16) as

$$\begin{aligned} |\mathcal{I}[l]| &= \left| \frac{\sin[\pi(i_1 - l + \epsilon)\tau/M]}{\sin[\pi(i_1 - l + \epsilon)/M]} \Phi_I \right. \\ &\quad \left. + \frac{\sin[\pi(i_2 - l + \epsilon)(M - \tau)/M]}{\sin[\pi(i_2 - l + \epsilon)/M]} \Phi_{II} \right| \\ &\leq \left| \frac{\sin[\pi(i_1 - l + \epsilon)\tau/M]}{\sin[\pi(i_1 - l + \epsilon)/M]} \right| \\ &\quad + \left| \frac{\sin[\pi(i_2 - l + \epsilon)(M - \tau)/M]}{\sin[\pi(i_2 - l + \epsilon)/M]} \right|. \end{aligned} \quad (54)$$

41 Let $\Lambda[l]$ denote the DFT output of the interfering signal
42 without the impact of fractional FO. According to [25], [37],
43 we have

$$\begin{aligned} |\Lambda[l]| &= \left| \frac{\sin[\pi(i_1 - l)\tau/M]}{\sin[\pi(i_1 - l)/M]} + \frac{\sin[\pi(i_2 - l)(M - \tau)/M]}{\sin[\pi(i_2 - l)/M]} \right| \\ &\leq \underbrace{\left| \frac{\sin[\pi(i_1 - l)\tau/M]}{\sin[\pi(i_1 - l)/M]} \right|}_{\Delta_I} \\ &\quad + \underbrace{\left| \frac{\sin[\pi(i_2 - l)(M - \tau)/M]}{\sin[\pi(i_2 - l)/M]} \right|}_{\Delta_{II}}. \end{aligned} \quad (55)$$

56 Since the function $\sin(Ax)/\sin(x)$ reaches its maximum
57 value A when $x \rightarrow 0$, Δ_I and Δ_{II} have maximum values τ
58 and $M - \tau$ at $l = i_1$ and $l = i_2$, respectively. Without loss of

59 generality, we assume $0 \leq \tau < \frac{M}{2}$ and hence, the maximum
60 value for (55) is more likely to occur at $l = i_2$, expressed as

$$\max_{l \in \mathcal{L}} \{|\Lambda[l]|\} \approx |\Lambda[i_2]| = \left| \frac{\sin[\pi(i_1 - i_2)\tau/M]}{\sin[\pi(i_1 - i_2)/M]} \right| + M - \tau. \quad (56)$$

61 Moreover, as pointed out in [32], the fractional FO ϵ leads
62 to energy spread in the DFT output, where the energy of the
63 interference peak diffuses into other frequency bins due to the
64 lack of DFT resolution. Namely, we have

$$\max_{l \in \mathcal{L}} \{|\mathcal{I}[l]|\} \leq \max_{l \in \mathcal{L}} \{|\Lambda[l]|\}. \quad (57)$$

65 Therefore, let $\chi = |i_1 - i_2|$ and thus we have

$$\begin{aligned} |\mathcal{I}[l]| &\leq \max_{l \in \mathcal{L}} \{|\mathcal{I}[l]|\} \leq \max_{l \in \mathcal{L}} \{|\Lambda[l]|\} \\ &\approx \left| \frac{\sin(\pi\chi\tau/M)}{\sin(\pi\chi/M)} \right| + M - \tau = \Lambda_{\chi,\tau}. \end{aligned} \quad (58)$$

66 The proof is completed.

REFERENCES

- [1] Q. Yu, D. Mishra, H. Wang, D. He, J. Yuan, and M. Matthaiou, "On the analytical error performance of LoRa-based LEO satellite IoT," submitted to *IEEE GLOBECOM 2025*.
- [2] M. Centenaro, C. E. Costa, F. Granelli, C. Sacchi, and L. Vangelista, "A survey on technologies, standards and open challenges in satellite IoT," *IEEE Commun. Surveys Tuts.*, vol. 23, no. 3, pp. 1693-1720, 3rd Quart., 2021.
- [3] M. Asad Ullah, K. Mikhaylov, and H. Alves, "Massive machine-type communication and satellite integration for remote areas," *IEEE Wireless Commun.*, vol. 28, no. 4, pp. 74-80, Aug. 2021.
- [4] J. A. Fraire, O. Iova, and F. Valois, "Space-terrestrial integrated Internet of things: Challenges and opportunities," *IEEE Commun. Mag.*, vol. 60, no. 12, pp. 64-70, Dec. 2022.
- [5] A. A. Doroshkin, A. M. Zadorozhny, O. N. Kus, V. Y. Prokopyev, and Y. M. Prokopyev, "Experimental study of LoRa modulation immunity to Doppler effect in CubeSat radio communications," *IEEE Access*, vol. 7, pp. 75721-75731, May 2019.
- [6] A. M. Zadorozhny *et al.*, "First flight-testing of LoRa modulation in satellite radio communications in low-Earth orbit," *IEEE Access*, vol. 10, pp. 100006-100023, Sep. 2022.
- [7] L. Fernandez, J. A. Ruiz-De-Azua, A. Calveras, and A. Camps, "Assessing LoRa for satellite-to-Earth communications considering the impact of ionospheric scintillation," *IEEE Access*, vol. 8, pp. 165570-165582, Sep. 2020.
- [8] G. M. Capez, S. Henn, J. A. Fraire, and R. Garello, "Sparse satellite constellation design for global and regional direct-to-satellite IoT services," *IEEE Trans. Aerosp. Electron. Syst.*, vol. 58, no. 5, pp. 3786-3801, Oct. 2022.
- [9] Y. Qian, L. Ma, and X. Liang, "Symmetry chirp spread spectrum modulation used in LEO satellite Internet of things," *IEEE Commun. Lett.*, vol. 22, no. 11, pp. 2230-2233, Nov. 2018.
- [10] A. Roy, H. B. Nemade, and R. Bhattacharjee, "Symmetry chirp modulation waveform design for LEO satellite IoT communication," *IEEE Commun. Lett.*, vol. 23, no. 10, pp. 1836-1839, Oct. 2019.
- [11] C. Yang, M. Wang, L. Zheng, and G. Zhou, "Folded chirp-rate shift keying modulation for LEO satellite IoT," *IEEE Access*, vol. 7, pp. 99451-99461, Jul. 2019.
- [12] Y. Qian, L. Ma, and X. Liang, "The performance of chirp signal used in LEO satellite Internet of things," *IEEE Commun. Lett.*, vol. 23, no. 8, pp. 1319-1322, Aug. 2019.
- [13] Y. Qian, L. Ma, and X. Liang, "The acquisition method of symmetry chirp signal used in LEO satellite Internet of things," *IEEE Commun. Lett.*, vol. 23, no. 9, pp. 1572-1575, Sept. 2019.
- [14] G. Colavolpe, T. Foggi, M. Ricciulli, Y. Zanettini, and J. -P. Medianio-Alameda, "Reception of LoRa signals from LEO satellites," *IEEE Trans. Aerosp. Electron. Syst.*, vol. 55, no. 6, pp. 3587-3602, Dec. 2019.

- [15] K. Dakic, B. Al Homssi, S. Walia, and A. Al-Hourani, "Spiking neural networks for detecting satellite Internet of things signals," *IEEE Trans. Aerosp. Electron. Syst.*, vol. 60, no. 1, pp. 1224-1238, Feb. 2024.
- [16] M. Magnant, B. Le Gal, G. Ferré, and F. Collard, "Implementation of a low Earth orbit satellite chirped preamble detector," *IEEE Trans. Aerosp. Electron. Syst.*, vol. 60, no. 6, pp. 8458-8469, Dec. 2024.
- [17] M. Afhamisis and M. R. Palattella, "SALSA: A scheduling algorithm for LoRa to LEO satellites," *IEEE Access*, vol. 10, pp. 11608-11615, Jan. 2022.
- [18] F. A. Tondo, M. Afhamisis, S. Montejos-Sánchez, O. L. A. López, M. R. Palattella, and R. D. Souza, "Multiple channel LoRa-to-LEO scheduling for direct-to-satellite IoT," *IEEE Access*, vol. 12, pp. 30627-30637, Feb. 2024.
- [19] S. Herrera-Alonso, M. Rodríguez-Pérez, R. F. Rodríguez-Rubio, and F. Pérez-Fontán, "Improving uplink scalability of LoRa-based direct-to-satellite IoT networks," *IEEE Internet Things J.*, vol. 11, no. 7, pp. 12526-12535, Apr. 2024.
- [20] L. Vangelista, "Frequency shift chirp modulation: The LoRa modulation," *IEEE Signal Process. Lett.*, vol. 24, no. 12, pp. 1818-1821, Dec. 2017.
- [21] M. Chiani and A. Elzanaty, "On the LoRa modulation for IoT: Waveform properties and spectral analysis," *IEEE Internet Things J.*, vol. 6, no. 5, pp. 8463-8470, Oct. 2019.
- [22] G. Pasolini, "On the LoRa chirp spread spectrum modulation: Signal properties and their impact on transmitter and receiver architectures," *IEEE Trans. Wireless Commun.*, vol. 21, no. 1, pp. 357-369, Jan. 2022.
- [23] B. Reinders and S. Pollin, "Chirp spread spectrum as a modulation technique for long range communication," in *Proc. IEEE SCVT*, Nov. 2016, pp. 1-5.
- [24] T. Elshabrawy and J. Robert, "Closed-form approximation of LoRa modulation BER performance," *IEEE Commun. Lett.*, vol. 22, no. 9, pp. 1778-1781, Sept. 2018.
- [25] T. Elshabrawy and J. Robert, "Analysis of BER and coverage performance of LoRa modulation under same spreading factor interference," in *Proc. IEEE PIMRC*, Sep. 2018, pp. 1-6.
- [26] O. Afisiadis, M. Cotting, A. Burg, and A. Balatsoukas-Stimming, "On the error rate of the LoRa modulation with interference," *IEEE Trans. Wireless Commun.*, vol. 19, no. 2, pp. 1292-1304, Feb. 2020.
- [27] C. F. Dias, E. R. de Lima, and G. Fraidenraich, "Bit error rate closed-form expressions for LoRa systems under Nakagami and Rice fading channels," *Sensors*, vol. 19, no. 20, p. 4412, Oct. 2019.
- [28] J. Courjault, B. Vrigneau, O. Berder, and M. R. Bhatnagar, "A computable form for LoRa performance estimation: Application to Ricean and Nakagami fading," *IEEE Access*, vol. 9, pp. 81601-81611, Apr. 2021.
- [29] K. Peppas, S. K. Chronopoulos, D. Loukatos, and K. Arvanitis, "New results for the error rate performance of LoRa systems over fading channels," *Sensors*, no. 22, vol. 3350, pp. 20, Apr. 2022.
- [30] C. Demeslay, P. Rostaing, and R. Gautier, "Theoretical performance of LoRa system in multipath and interference channels," *IEEE Internet Things J.*, vol. 9, no. 9, pp. 6830-6843, May 2022.
- [31] J. Liu, Y. Yan, H. Yu, and B. Ma, "Approximate BER performance of LoRa modulation with heavy multipath interference," *IEEE Wireless Commun. Lett.*, vol. 12, no. 5, pp. 853-857, May 2023.
- [32] P. Huang, J. Liu, and B. Ma, "Approximate BER performance of LoRa communication under carrier frequency offset," *IEEE Internet Things J.*, vol. 11, no. 15, pp. 26001-26004, Aug. 2024.
- [33] H. Ma, G. Cai, Y. Fang, P. Chen, and G. Han, "Design and performance analysis of a new STBC-MIMO LoRa system," *IEEE Trans. Commun.*, vol. 69, no. 9, pp. 5744-5757, Sept. 2021.
- [34] W. Xu, G. Cai, Y. Fang, S. Mumtaz, and G. Chen, "Performance analysis and resource allocation for a relaying LoRa system considering random nodal distances," *IEEE Trans. Commun.*, vol. 70, no. 3, pp. 1638-1652, Mar. 2022.
- [35] G. Lin, A. Elzanaty, and M. -S. Alouini, "LoRa backscatter communications: Temporal, spectral, and error performance analysis," *IEEE Internet Things J.*, vol. 10, no. 18, pp. 16412-16426, Sept. 2023.
- [36] X. Zhang, W. Xu, G. Cai, Y. Song, and G. Chen, "A new reconfigurable intelligent-surface-assisted LoRa system," *IEEE Trans. Veh. Technol.*, vol. 71, no. 8, pp. 9055-9060, Aug. 2022.
- [37] Z. Liang, G. Cai, J. He, G. Kaddoum, C. Huang, and M. Debbah, "RIS-enabled anti-interference in LoRa systems," *IEEE Trans. Commun.*, vol. 72, no. 10, pp. 6599-6616, Oct. 2024.
- [38] Z. Liang, G. Cai, J. He, G. Kaddoum, and C. Huang, "Performance analysis of multi-RIS-aided LoRa systems with outdated and imperfect CSI," *IEEE Trans. Commun.*, early access.
- [39] L. Bariah, W. Jaafar, S. Muhaidat, H. Elgala, and H. Yanikomeroglu, "On the error performance of LoRa-enabled aerial networks over shadowed Rician fading channels," *IEEE Commun. Lett.*, vol. 26, no. 10, pp. 2322-2326, Oct. 2022.
- [40] Q. Yu, H. Wang, D. He, and Z. Lu, "Enhanced group-based chirp spread spectrum modulation: Design and performance analysis," *IEEE Internet Things J.*, vol. 12, no. 5, pp. 5079-5092, Mar. 2025.
- [41] D. Croce, M. Guicciardo, S. Mangione, G. Santaromita, and I. Tinnirello, "Impact of LoRa imperfect orthogonality: Analysis of link-level performance," *IEEE Commun. Lett.*, vol. 22, no. 4, pp. 796-799, Apr. 2018.
- [42] L. -T. Tu, A. Bradai, Y. Poussot, and A. I. Aravanis, "On the spectral efficiency of LoRa networks: Performance analysis, trends and optimal points of operation," *IEEE Trans. Commun.*, vol. 70, no. 4, pp. 2788-2804, Apr. 2022.
- [43] A. Al-Hourani, "An analytic approach for modeling the coverage performance of dense satellite networks," *IEEE Wireless Commun. Lett.*, vol. 10, no. 4, pp. 897-901, Apr. 2021.
- [44] B. Al Homssi and A. Al-Hourani, "Optimal beamwidth and altitude for maximal uplink coverage in satellite networks," *IEEE Wireless Commun. Lett.*, vol. 11, no. 4, pp. 771-775, Apr. 2022.
- [45] A. Al-Hourani and I. Guvene, "On modeling satellite-to-ground path-loss in urban environments," *IEEE Commun. Lett.*, vol. 25, no. 3, pp. 696-700, Mar. 2021.
- [46] V. Savaux, C. Delacourt, and P. Savelli, "On time-frequency synchronization in LoRa system: From analysis to near-optimal algorithm," *IEEE Internet Things J.*, vol. 9, no. 12, pp. 10200-10211, Jun. 2022.
- [47] L. Vangelista and A. Cattapan, "Start of packet detection and synchronization for LoRaWAN modulated signals," *IEEE Trans. Wireless Commun.*, vol. 21, no. 6, pp. 4608-4621, Jun. 2022.
- [48] S. An, Z. Lu, H. Wang, and Q. Yu, "A turbo coded LoRa-index modulation scheme for IoT communication," in *Proc. IEEE ICCT*, Oct. 2021, pp. 736-740.
- [49] R. Wang and J. Bao, "ELLR-BP: An enhanced LLR BP algorithm based on LDPC coding for LoRa physical layer," *IEEE Trans. Green Commun. Netw.*, early access.
- [50] A. A. Tesfay, S. Kharbech, E. P. Simon, and L. Clavier, "Signal denoising and detection for uplink in LoRa networks based on Bayesian-optimized deep neural networks," *IEEE Commun. Lett.*, vol. 27, no. 1, pp. 214-218, Jan. 2023.
- [51] J. Huang and G. Cai, "Joint channel estimation and signal detection for LoRa systems using convolutional neural network," *IEEE Commun. Lett.*, vol. 28, no. 3, pp. 662-666, Mar. 2024.
- [52] A. Jeffrey and D. Zwillinger, *Table of Integrals, Series, and Products*. Amsterdam, The Netherlands: Elsevier, 2007.